RESEARCH ARTICLE

CHEMISTRY

Improving photosensitization for photochemical CO$_2$-to-CO conversion

Ping Wang[1], Ru Dong[1], Song Guo[1,*], Jianzhang Zhao[2], Zhi-Ming Zhang [ID][1,*] and Tong-Bu Lu[1]

ABSTRACT

Inspired by nature, improving photosensitization represents a vital direction for the development of artificial photosynthesis. The sensitization ability of photosensitizers (PSs) reflects in their electron-transfer ability, which highly depends on their excited-state lifetime and redox potential. Herein, for the first time, we put forward a facile strategy to improve sensitizing ability via finely tuning the excited state of Ru(II)-PSs (**Ru-1**–**Ru-4**) for efficient CO$_2$ reduction. Remarkably, [Ru(Phen)$_2$(3-pyrenylPhen)]$^{2+}$ (**Ru-3**) exhibits the best sensitizing ability among **Ru-1**–**Ru-4**, over 17 times higher than that of typical Ru(Phen)$_3$$^{2+}$. It can efficiently sensitize a dinuclear cobalt catalyst for CO$_2$-to-CO conversion with a maximum turnover number of 66 480. Systematic investigations demonstrate that its long-lived excited state and suitable redox driving force greatly contributed to this superior sensitizing ability. This work provides a new insight into dramatically boosting photocatalytic CO$_2$ reduction via improving photosensitization.

Keywords: photosensitization, photocatalysis, CO$_2$ reduction, excited state, Ru(II) complexes

[1]MOE International Joint Laboratory of Materials Microstructure, Institute for New Energy Materials and Low Carbon Technologies, School of Materials Science and Engineering, Tianjin University of Technology, Tianjin 300384, China and [2]State Key Laboratory of Fine Chemicals, School of Chemical Engineering, Dalian University of Technology, Dalian 116024, China

*Corresponding authors. E-mails: guosong@email.tjut.edu.cn; zmzhang@email.tjut.edu.cn

INTRODUCTION

Solar-driven reduction of CO$_2$ into energy-rich fuels, such as CO, HCOOH and CH$_3$OH, has been conceived of as a highly promising approach to solve the energy crisis and environmental pollution [1–6]. In the past decades, great efforts have long been devoted to improving the photocatalytic activity and selectivity for efficient CO$_2$ conversion. Throughout the molecular photocatalytic systems, numerous catalysts, such as complexes of Re, Ru, Fe, Co and Ni, have been developed [7–13] with detailed study of their catalytic mechanism [14–17]. In light of their being relatively comprehensively studied, more and more attention has begun to shift to accelerate electron transfer between catalyst and antenna molecules to promote CO$_2$ reduction. For example, Ishitani and several groups have explored efficient photocatalytic systems through combining photosensitizers (PSs) with catalysts via covalent bonds [8,9,18–20]. These systems exhibited enhanced catalytic ability compared to that of separated systems owing to their more efficient electron transfer via intramolecular process. However, this strategy was limited by the complex synthesis and lack of flexibility in investigating different PSs and catalysts. Very recently, Cheung *et al.* discovered that the hydrogen-bonding interaction between PSs and catalysts can improve the catalytic performance [21]. Nevertheless, these H-bonds can be easily disrupted by external factors, e.g. temperature and the solvents of N,N-Dimethylformamide (DMF) and H$_2$O. Accordingly, it is highly necessary yet remains greatly challenging to develop an alternative strategy for dramatically boosting photocatalytic CO$_2$ reduction (Fig. 1).

PSs, as the light-harvesting main body, have been widely used as a key mediator for efficient electron transfer between catalysts and electron donors in both natural and artificial photosynthetic systems [3,9,22–24]. Currently, improving the photosensitization ability of PSs for enhancing photocatalytic performance for CO$_2$ reduction is still in its infancy [24,25]. In this field, the frequently used PSs were confined to prototypical metal-to-ligand charge-transfer complexes [24,26–30], such as Ru(bpy)$_3$$^{2+}$ [31–34] and Ru(Phen)$_3$$^{2+}$ (Phen = 1,10-phenanthroline) [35–37], where their
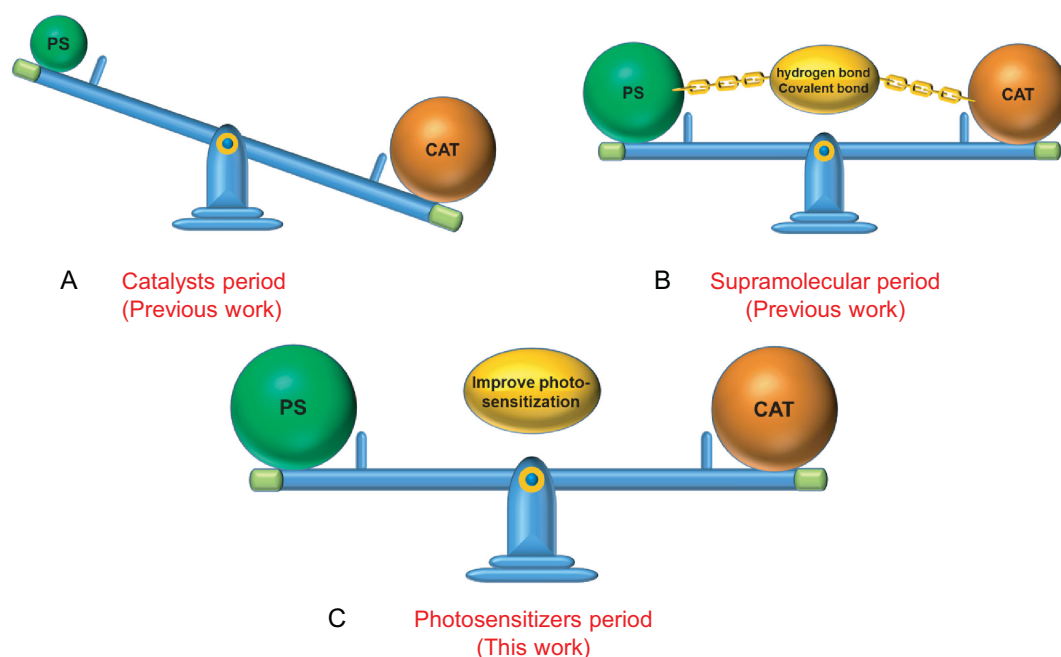
Figure 1. Evolution process of the photocatalytic system for CO_2 reduction. (A) The study was mainly focused on the development of highly active catalysts (CATs) during this period. (B) Non-covalent/covalent supramolecular assembly has been developed over the past decades. (C) In this work, we open a new way to boost photocatalytic CO_2 reduction by improving the photosensitization ability of photosensitizers (PSs).

excited-state lifetime was usually $<1\,\mu s$ ($\tau = 600$ ns for $Ru(bpy)_3^{2+}$ and 360 ns for $Ru(Phen)_3^{2+}$ in CH_3CN) [36,38,39]. It will be a promising way to boost CO_2 reduction via adjusting the excited-state population and lifetime of these PSs to improve their sensitizing ability. In the past decades, decreasing the energy level of organic ligands by implanting a conjugated group has been used as a common strategy for achieving a long-lived excited state, which can realize a transition from ^{3}MLCT state to ^{3}IL state (intraligand triplet excited state) [40–45]. In this field, we have first introduced ^{3}IL-type PSs with a long-lived excited state into photocatalytic systems for efficient H_2 production [43,45]. Unfortunately, the excited oxidation potentials of PSs usually become more positive in this process. This will greatly weaken the driving force for electron transfer from excited PSs to catalysts in thermodynamic catalytic processes [44,45]. As a result, how to substantially improve the sensitizing ability of molecular antenna whilst balancing its excited-state lifetime and redox driving force represents a key role in enhancing photoconversion efficiency, although it still remains a great challenge.

In this contribution, we put forward a new strategy to greatly boost photocatalytic CO_2 reduction by improving the photosensitization ability of PSs. A family of Ru(II)-based PSs **Ru-2**, **Ru-3** and **Ru-4** were prepared by the selective addition of pyrene/pyrenyl ethynylene to the 3- and 5-positions

of Phen in $Ru(Phen)_3^{2+}$ (**Ru-1**) (Supplementary Figs 1–18). The triplet lifetimes of these complexes were gradually prolonged and their excited-state oxidation potentials became less negative with fine-tuning the excited state from **Ru-1** with the ^{3}MLCT state to **Ru-4** with the ^{3}IL state, which provided a platform to compare the effect of PSs with different sensitizing abilities on photocatalytic CO_2 reduction. Remarkably, the most efficient PS **Ru-3** simultaneously possesses a long triplet lifetime (68.2 μs), $\sim$189 times longer than that of $Ru(Phen)_3^{2+}$, and a suitable excited-state oxidation potential (-0.92 V *vs* Saturated Calomel Electrode (SCE)). Impressively, the sensitizing ability of **Ru-3** is >17 times higher than that of typical **Ru-1** and it can efficiently sensitize the dinuclear cobalt catalyst (**C-1**) for photochemical CO_2-to-CO conversion with an extremely high TON of 66 480.

RESULTS

Molecular design and optical properties

In order to achieve a more rational molecular design, Gaussian calculations were carefully performed to predict the energy level of the triplet states and molecular geometries of the pyrene–phen ligands **L-2**–**L-4** and **Ru-1**–**Ru-4** (Fig. 2, Supplementary Figs 19 and 20, and Supplementary Table 1). As shown in Fig. 2A, the triplet energy levels of these ligands
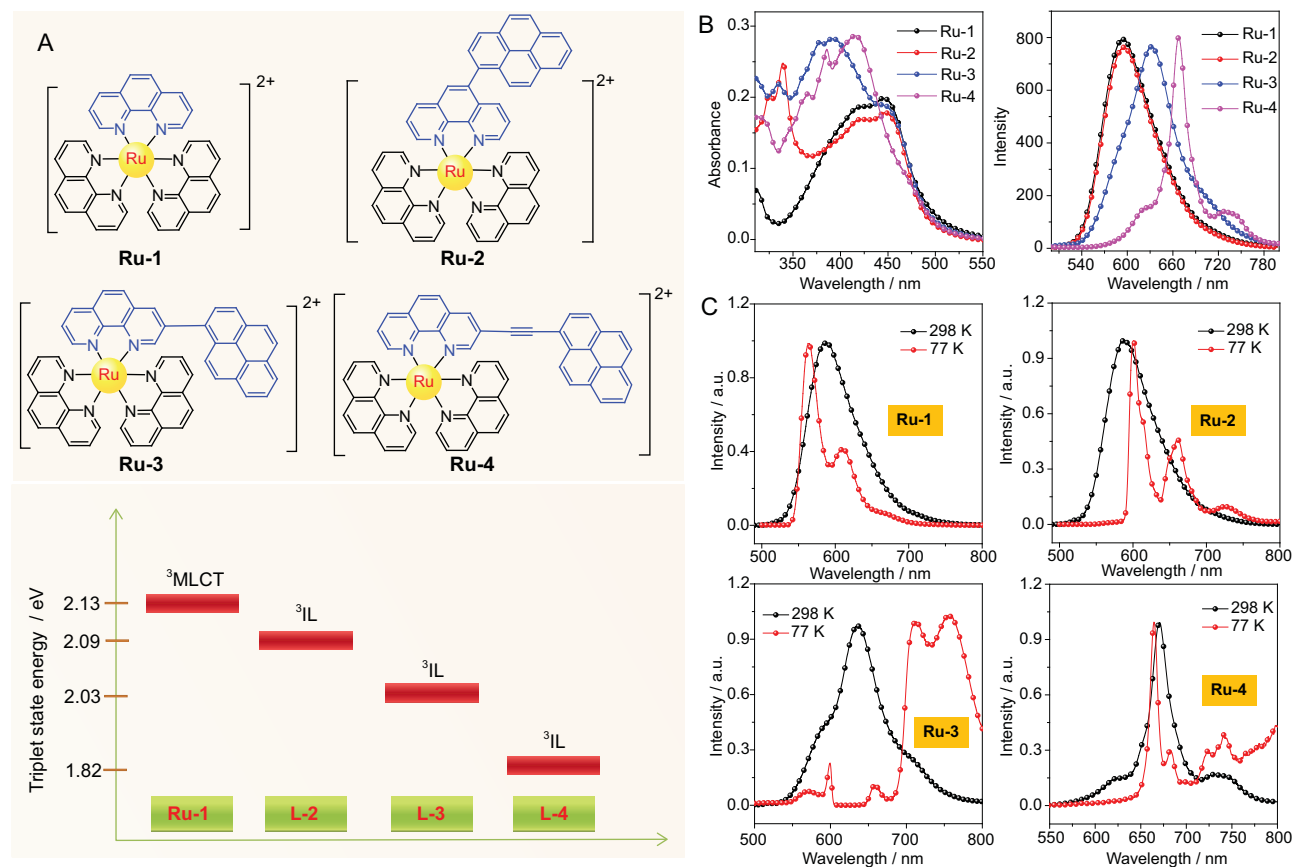
Figure 2. Fine-tuning the excited state of PSs to improve photosensitization for photochemical CO_2-to-CO conversion. (A) Molecular structure of **Ru-1**–**Ru-4** (up). Energy diagram of triplet states of **Ru-1** and **L-2**–**L-4**, calculated at the B3LYP/6–31 G/genecp/LanL2DZ level with Gaussian O9 W (down). (B) UV-vis absorption and emission spectra of **Ru-1**–**Ru-4** under the same condition, λ_{ex} = 450 nm, c = 5.0 μM in deaerated CH_3CN. (C) Emission spectra of Ru(II) complexes at RT and 77 K: **Ru-1**, λ_{ex} = 450 nm; **Ru-2**, λ_{ex} = 450 nm; **Ru-3**, λ_{ex} = 450 nm; **Ru-4**, λ_{ex} = 450 nm.

were in the order of **L-2** > **L-3** > **L-4**, which was proportional to the dihedral angle between phen and pyrene ($71°$ for **L-2** > $55°$ for **L-3** > $0°$ for **L-4**) (Supplementary Figs 19 and 20, and Supplementary Table 1). Meanwhile, the energy level of the ^{3}IL states of these ligands was lower than that of the ^{3}MLCT state of $Ru(Phen)_3{}^{2+}$, indicating that the triplet states of pyrene-functionalized Ru(II) complexes will be mainly localized on the pyrene–phen ligands (^{3}IL states). Hence, fine-tuning the excited states is promising to be achieved by adjusting the position of pyrenyl on Phen of Ru(II) complexes.

According to Density Functional Theory (DFT) calculations, **Ru-2**–**Ru-4** were predicted as ideal models to determine the effect of the excited states on their sensitizing ability due to their well-proportioned energy-level gradient. All these complexes were synthesized according to the modified literature methods described in Supplementary Scheme 1 [42,46]. In this synthetic process, the precursors **L-2**, **L-3** and **L-4** were prepared by selective bromination of phen and

subsequent coupling with pyrenylboronic acid and ethynyl pyrene, which were used to coordinate with Ru^{3+} to generate corresponding **Ru-2**–**Ru-4** via a one-pot reaction, respectively. These complexes and intermediates were fully characterized by ^{1}H NMR, ^{13}C NMR and MS spectroscopy (Supplementary Figs 1–18).

The UV-vis absorption spectra of **Ru-1**–**Ru-4** are presented in Fig. 2B. **Ru-1** exhibits an absorption band of between 400 and 500 nm, corresponding to $S_o \rightarrow {}^1$MLCT transition. For pyrene, a dual peak was observed at 319 and 334 nm, respectively, arising from $\pi \rightarrow \pi^*$ transition (Supplementary Fig. 21). The absorption spectrum of **Ru-2** is almost a superposition of that of **Ru-1** and pyrene, indicating a weak electron communication between $Ru(Phen)_3{}^{2+}$ and pyrenyl at the ground state [45]. In contrast to the absorption of **Ru-1** and **Ru-2**, a new peak at around 380 and 400 nm emerged in the absorption spectra of **Ru-3** and **Ru-4**, respectively, which resulted from the strong electronic interaction between the Ru center and pyrenyl. Interestingly, **Ru-3** and **Ru-4** exhibit a stronger

visible-light-absorption ability than that of **Ru-1** and **Ru-2**. As a result, molecular regulation can gradually enhance the electron communication between $Ru(Phen)_3^{2+}$ and pyrenyl from **Ru-2** to **Ru-4**. Moreover, the absorption spectra of **Ru-1**–**Ru-4** in the presence of **C-1** or **TEOA** were almost similar to that of PSs alone (Supplementary Fig. 22). These results reveal that there is no intermolecular electronic interaction between the PSs under ground state and **C-1** (or **TEOA**) [45,47].

The photoluminescence (PL) spectra of **Ru-1**–**Ru-4** were carried out to investigate their excited-state properties (Fig. 2B and Supplementary Fig. 23). As shown in Supplementary Fig. 23, all the peaks in the PL spectra of **Ru-1**–**Ru-4** that emerged under the Ar atmosphere were significantly quenched as exposed to air, indicating the phosphorescence emission process, which mainly derived from the triplet state [48,49]. The PL spectrum of **Ru-1** showed a typical ^{3}MLCT emission at 595 nm and a similar emission peak at 595 nm was also observed in the PL spectrum of **Ru-2**, manifesting that its ^{3}MLCT characteristic in **Ru-2** partially remained after molecular regulation. In the PL spectra of **Ru-3** and **Ru-4**, a redshift and much broader phosphorescence emission at around 632 and 668 nm was presented in comparison with that of **Ru-1**. Especially for **Ru-4**, its emission reveals a fine structure and an obvious shoulder peak at 735 nm, indicating the existence of an ^{3}IL emissive state. The emissive state of **Ru-3** should stand between those of **Ru-2** and **Ru-4**. All the above results were further illuminated by 77 K emission and nanosecond transient absorption spectra.

The emission spectra of **Ru-1**–**Ru-4** at 77 and 298 K were compared for clarifying their emissive state (Fig. 2C). A large hypochromic shift between 77 and 298 K spectra was observed for **Ru-1** (ΔE_s, 665.7 cm^{-1}), indicating a typical ^{3}MLCT emissive state [48,50]. By contrast, **Ru-4** showed a small hypochromic shift at 670 nm (148.7 cm^{-1}), suggesting an ^{3}IL emissive state. For **Ru-2**, an emission band between 600 and 800 nm was observed at 77 K, which matched well with the phosphorescence of pyrene [51]. Thus, this indicated a pyrenyl localized emissive state. Interestingly, the PL spectrum of **Ru-3** exhibits multiple emission peaks at 77 K. Two weak peaks at around 600 and 660 nm close to the pyrenyl localized emissive state of **Ru-2** were detected in the PL spectrum of **Ru-3** and a strong dual emission around 750 nm that corresponded to the ^{3}IL emissive state was also observed. This dual emission also emerged in the PL spectrum of **Ru-4**. As a result, it can be proposed that the emissive state of **Ru-3** was between those of **Ru-2** and **Ru-4**, but was dominated by the ^{3}IL emissive state.

To further decipher their excited-state properties, nanosecond transient absorption spectra were performed on these four PSs, **Ru-1**–**Ru-4** (Fig. 3A–D). The transient spectrum of **Ru-1** showed a bleaching band at around 450 nm corresponding to the depletion of the ground state, which was a typical characteristic of the ^{3}MLCT state. In the transient spectra of **Ru-2**–**Ru-4**, there was some superposition between the bleaching band and the excited-state absorption band [48]. **Ru-2** only afforded a transient absorption band between 380 and 700 nm, along with its ^{3}MLCT emission at 595 nm; thus, its excited state could be ascribed to a mix of ^{3}MLCT and the pyrenyl localized excited state. The transient spectrum of **Ru-3** shows a positive absorption above 400 nm and a bleaching peak at 371 nm, manifesting a feature of the ^{3}IL state. For **Ru-4**, a strong bleaching band at around 400 nm was observed, which matched well with its steady absorption to re-affirm its ^{3}IL state.

Spin-density surfaces of these Ru(II) complexes (**Ru-1**–**Ru-4**) were calculated at B3LYP/6–31 G/genecp/LanL2DZ level with Gaussian 09, which can rationalize the population of their triplet states. As shown in Fig. 3, the spin density of **Ru-1** was primarily localized on the Ru-Phen coordination center, indicative of a ^{3}MLCT state. For **Ru-2**–**Ru-4**, their spin densities were mainly distributed on the Phen and pyrene owing to the lower triplet energy level of pyrenyl-Phen than that of the ^{3}MLCT state. These results supported that the excited states of **Ru-2**–**Ru-4** were largely populated on the ligands, which matched well with the experimental results. Therefore, we proposed that the redox center should be localized at pyrenyl functionalized ligands. All the photophysical data are summarized in Table 1 and the combination of these data with these calculated results can illustrate that fine-tuning of the excited state of these PSs from ^{3}MLCT state to the ^{3}IL state was realized. This provided a platform on which to compare the effect of PSs with different sensitizing abilities on photocatalytic CO_2 reduction.

Photocatalytic CO$_2$ reduction

Further, to reveal the influence of different sensitizing abilities on CO_2 reduction, photocatalytic activities of these Ru(II) complexes (**Ru-1**–**Ru-4**) were investigated in 5 mL CO_2-saturated CH_3CN/H_2O (v/v = 9/1) solution containing **C-1** as the catalyst and **TEOA** as the electron sacrificial agent under the illumination of a 450 nm LED (Fig. 4 and Supplementary Tables 2–4). As shown in Fig. 4A, the TON of **C-1** with **Ru-3** was up to 1120, 17 times higher
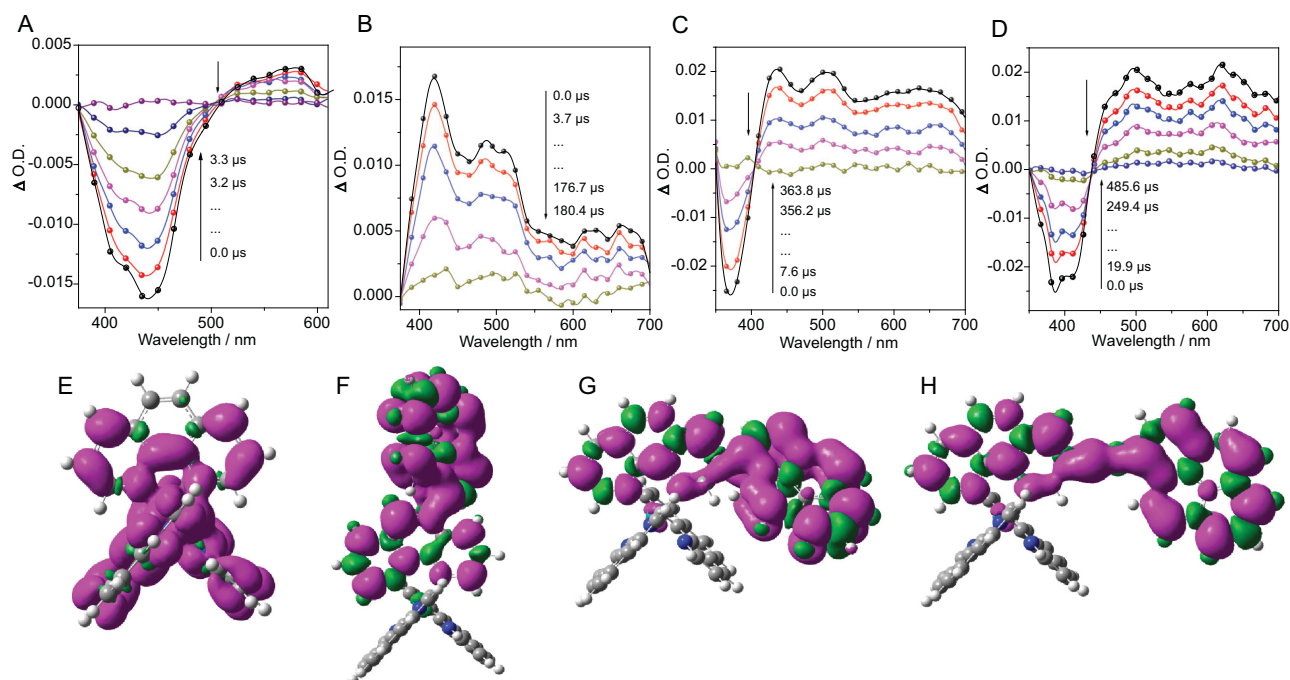
Figure 3. The triplet excited-state population of PSs. Nanosecond time-resolved transient difference absorption spectra of (A) **Ru-1**, (B) **Ru-2**, (C) **Ru-3** and (D) **Ru-4**. After pulsed excitation at 450 nm for **Ru-1** and **Ru-4**, 355 nm for **Ru-2** and **Ru-3** (c_{PS} = 5 μM in deaerated CH_3CN). Spin-density surface of (E) **Ru-1**, (F) **Ru-2**, (G) **Ru-3** and (H) **Ru-4**. Calculated at the B3LYP/6–31 G/genecp/LanL2DZ level with Gaussian 09 W.

than that with **Ru-1**. In the **Ru-3**-containing photocatalyic system, the TON towards **C-1** can reach as high as 66 480 under the optimized condition, which substantially exceeds our previously reported results with **Ru-1** as the PS (TON = 16 896, Supplementary Table 3) [35]. In addition, no or a trace amount of CO was detected in the absence of PS, **TEOA**, **C-1**, light or CO_2, manifesting that all the above factors are indispensable for efficient photocatalytic CO_2 reduction (Supplementary Table 4).

The photocatalytic mechanism was studied by steady and transient quenching experiments (Fig. 4). Phosphorescence quenching experiments of **Ru-1**–**Ru-4** reveal that their excited states can be efficiently quenched by **C-1**; nevertheless, no change on their photoluminescence spectra was observed in the presence of **TEOA** (Supplementary Figs 24 and 25). We therefore proposed that the photocatalytic process was dominated by the oxidation mechanism

for **Ru-1**–**Ru-4**-containing systems [35,36], which was further confirmed by nanosecond transient absorption. The triplet lifetimes of **Ru-1**–**Ru-4** remained before and after adding to **TEOA**, but became shorter in the presence of **C-1**, confirming that the initial step for electron transfer should be from excited PSs to **C-1** (Fig. 4B and Supplementary Fig. 26). As a result, all these photocatalytic systems could be determined as oxidation mechanisms (Fig. 4C).

With the above results in mind, both triplet excited-state lifetimes and the excited-state oxidation potentials of PSs are key factors affecting electron-transfer efficiency in photocatalytic systems. From the view of kinetics, the long-lived triplet state of PSs greatly contributed to intermolecular electron transfer/energy transfer. Thus, Stern–Volmer-quenching constants of PSs by **C-1** were in the order of 4.4×10^3 M^{-1} for **Ru-4** > 3.2 ×

Table 1. Summary of photophysical data of **Ru-1**–**Ru-4**.[a]

	λ_{abs}/nm	λ_{em}/nm	ε/(M^{-1} cm^{-1})	τ/μs[b]	K_1/(M^{-1})[c]
Ru-1	447	595	20 914	0.4	375
Ru-2	447	595	19 824	32.0	957
Ru-3	391	632	33 318	68.2	3239
Ru-4	415	668	49 808	118.7	4419

[a] 5.0 μM **Ru-1**–**Ru-4** in CH_3CN. [b] Triplet excited-state lifetime measured by transient absorption. [c] Stern–Volmer-quenching constants with **C-1** as the quenchers.
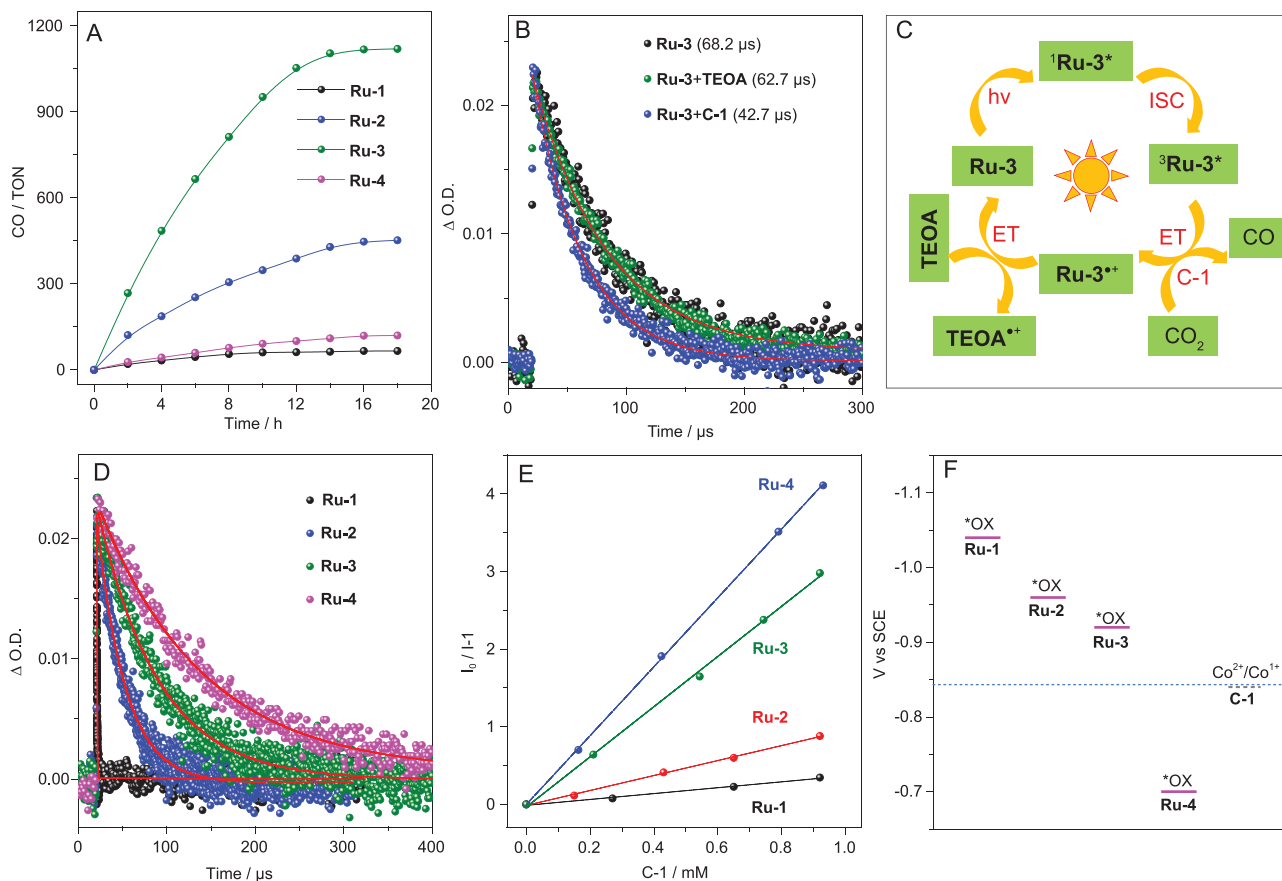
Figure 4. Photocatalytic CO_2 reduction and photocatalytic mechanism. (A) Photocatalytic CO_2 reduction with **Ru-1**–**Ru-4** under irradiation of a LED light (450 nm, 100 mW cm^{-2}, irradiation area, 0.8 cm^2) in the presence of PS (20 μM), **C-1** (1.0 μM) and **TEOA** (0.3 M) in 5 mL CO_2-saturated CH_3CN/H_2O ($v/v = 9/1$) solution. Each photocatalytic reaction was repeated at least three times. (B) Nanosecond transient absorption spectra of kinetic decay trace of **Ru-3** (black), **Ru-3** with 0.4 mM **TEOA** (green), and **Ru-3** with 0.5 μM **C-1** (blue). (C) Photocatalytic process with **Ru-3** as PS. ET, electron transfer; ISC, intersystem crossing. (D) Kinetic traces of **Ru-1**–**Ru-4** followed at 450 nm. (E) Stern–Volmer plot of **Ru-1**–**Ru-4**. λ_{ex} = 450 nm, c_{PS} = 5.0 μM. (F) Energy diagram depicting the excited-state oxidation potential (∗Ox) of **Ru-1**–**Ru-4** and the onset reduction potential of **C-1** in the catalytic system.

10^3 M^{-1} for **Ru-3** > 9.6 × 10^2 M^{-1} for **Ru-2** > 3.8 × 10^2 M^{-1} for **Ru-1**, which was proportional to their excited-state lifetimes (Fig. 4D and E). From the thermodynamics viewpoint, the excited-state oxidation potentials of PSs determine the driven force of electron transfer from excited PSs to **C-1** (Supplementary Table 5). As shown in Fig. 4F, the absolute value of the excited-state oxidation potential was in the order of **Ru-4** < **C-1** < **Ru-3** < **Ru-2** < **Ru-1**, indicating that excited **Ru-1**–**Ru-3** can provide a sufficient driven force for delivering the electron to **C-1** but the driven force from excited **Ru-4** to **C-1** was humble. Notably, the triple bond in **Ru-4** makes greater delocalization than **Ru-2** and **Ru-3**, indicating a lower excited-state energy level of the ligand in **Ru-4**. This delocalization can contribute to obtaining a long-lived excited state. However, the oxidizing ability of excited **Ru-4** becomes weaker, which is disadvantageous for electron transfer from excited **Ru-4** to **C-1** and will further decrease the photocatalytic

activity. As a result, **Ru-3**, as a trade-off PS, possesses a long-lived triplet state and a suitable excited-state oxidation potential simultaneously, highlighting its great potential for efficient CO_2 reduction.

CONCLUSION

In summary, we have developed a novel strategy to boost photocatalytic CO_2 reduction via improving photosensitization. In this work, four Ru-based complexes (**Ru-1**–**Ru-4**) were prepared and they presented a gradual variable excited state from **Ru-1** with the ^{3}MLCT state to **Ru-4** with the ^{3}IL state, which provides a platform on which to compare the effect of PSs with different sensitizing abilities on photocatalytic CO_2 reduction. Remarkably, the catalytic activity of **Ru-3** was >17 times higher than that of **Ru-1** and the TON towards **C-1** can reach 66 480. The outstanding photocatalytic activity of **Ru-3** was chiefly ascribed to its long-lived excited

state and suitable excited-state oxidation potential. This work provides a new insight into substantially improving visible-light-driven CO_2-reduction performance through fine-tuning the excited states of PSs on a molecular level.

METHODS

Materials and instrumentation

All the reactions were performed in argon unless otherwise mentioned. All the solvents were of analytical grade and distilled before use. The dichloro(p-cymene)ruthenium(II) dimer and 1,10-Phenanthroline were purchased from Sigma-Aldrich. The 1-pyrenylboronic acid, NH_4PF_6 and K_2CO_3 were purchased from HEOWNS. The Tetrakis(triphenylphosphine)palladium(0) and CuI were purchased from Adamas-beta. Chromatographic-grade acetonitrile was purchased from Adamas Reagent. The synthetic scheme of **Ru-1**–**Ru-4** is presented in Supplementary Scheme 1. The synthetic intermediates and target complexes were evidenced by ^{1}H NMR, ^{13}C NMR and mass spectroscopy. Elemental analysis was performed as C/H/N analyses on the Vario EL Cube (Elementar, Germany).

Electrochemical measurements were carried out on a CHI 760E electrochemical workstation at room temperature. The amount of CO product was analysed by gas chromatography (Shimadzu GC-2014+AT 230C, TDX-01 column, TCD, argon carrier). UV-vis absorption spectra were recorded on a LAMBDA750 UV-vis spectrophotometer. Fluorescence spectra were taken on a Hitachi F4600 spectrofluorometer. Transient absorption spectra were measured on the LP980 laser flash photolysis instrument (Edinburgh, UK).

Photocatalytic CO_2 reduction

Photocatalytic CO_2 reduction was conducted under 1 atm of CO_2 at 25°C in 5 mL reactor containing PS (20.0 μM), catalyst (1.0 μM), **TEOA** (0.3 M), 0.5 mL H_2O and 4.5 mL CH_3CN. The photocatalytic system was bubbled with CO_2 for 30 min. The mixture was continuously stirred and irradiated under a LED ($\lambda = 450$ nm, 100 mW cm^{-2}).

DFT calculation

The geometries and the spin-density surfaces of the complexes (**Ru-1**–**Ru-4**) were performed at the B3LYP/6–31 G/LanL2DZ level. There are no imaginary frequencies for all optimized structures of **L-1**–**L-4** and **Ru-1**–**Ru-4**. The triplet-state energy levels were carried out with the time-dependent DFT

(TDDFT) method. All these calculations were performed with Gaussian 09 W.

DATA AND SOFTWARE AVAILABILITY

All data needed to evaluate the conclusions in the paper are present in the paper and/or the Supplementary Materials. Additional data related to this paper may be requested from the authors.

SUPPLEMENTARY DATA

Supplementary data are available at *NSR* online.

FUNDING

AUTHOR CONTRIBUTIONS

S.G. and Z.M.Z. conceived of and designed this project, P.W. and R.D. performed the experiments, S.G. and J.Z. carried out the DFT calculation, P.W., S.G. and Z.M.Z. analysed the data, and P.W., S.G., J.Z., Z.M.Z. and T.B.L. wrote and revised the article.

Conflict of interest statement. None declared.

REFERENCES

1. Concepcion JJ, House RL and Papanikolas JM *et al.* Chemical approaches to artificial photosynthesis. *Proc Natl Acad Sci USA* 2012; **109**: 15560–4.

2. Aresta M, Dibenedetto A and Angelini A. Catalysis for the valorization of exhaust carbon: from CO_2 to chemicals, materials, and fuels. technological use of CO_2. *Chem Rev* 2014; **114**: 1709–42.

3. Morris AJ, Meyer GJ and Fujita E. Molecular approaches to the photocatalytic reduction of carbon dioxide for solar fuels. *Acc Chem Res* 2009; **42**: 1983–94.

4. Rosas-Hernandez A, Steinlechner C and Junge H *et al.* Photo- and electrochemical valorization of carbon dioxide using earth-abundant molecular catalysts. *Top Curr Chem* 2018; **376**: 229–53.

5. Corma A and Garcia H. Photocatalytic reduction of CO_2 for fuel production: possibilities and challenges. *J Catal* 2013; **308**: 168–75.

6. Li X, Yu J and Jaroniec M *et al.* Cocatalysts for selective photoreduction of CO_2 into solar fuels. *Chem Rev* 2019; **119**: 3962–4179.

7. Qiao X, Li Q and Schaugaard RN *et al.* Well-defined nanographene–rhenium complex as an efficient electrocatalyst and photocatalyst for selective CO_2 reduction. *J Am Chem Soc* 2017; **139**: 3934–7.

8. Kuriki R, Yamamoto M and Higuchi K *et al*. Robust binding between carbon nitride nanosheets and a binuclear Ru(II) complex enabling durable, selective CO_2 reduction under visible light in aqueous solution. *Angew Chem Int Ed* 2017; **56**: 4867–71.

9. Takeda H, Cometto C and Ishitani O *et al*. Electrons, photons, protons and earth-abundant metal complexes for molecular catalysis of CO_2 reduction. *ACS Catal* 2016; **7**: 70–88.

10. Guo Z, Chen G and Cometto C *et al*. Selectivity control of CO versus $HCOO^-$ production in the visible-light-driven catalytic reduction of CO_2 with two cooperative metal sites. *Nat Catal* 2019; **2**: 801–8.

11. Bonin J, Maurin A and Robert M. Molecular catalysis of the electrochemical and photochemical reduction of CO_2 with Fe and Co metal based complexes: recent advances. *Coord Chem Rev* 2017; **334**: 184–98.

12. Wang JW, Liu WJ and Zhong DC *et al*. Nickel complexes as molecular catalysts for water splitting and CO_2 reduction. *Coord Chem Rev* 2019; **378**: 237–61.

13. Kuramochi Y, Ishitani O and Ishida H. Reaction mechanisms of catalytic photochemical CO_2 reduction using Re(I) and Ru(II) complexes. *Coord Chem Rev* 2018; **373**: 333–56.

14. Clark ML, Cheung PL and Lessio M *et al*. Kinetic and mechanistic effects of bipyridine (bpy) substituent, labile ligand, and brønsted acid on electrocatalytic CO_2 reduction by Re(bpy) complexes. *ACS Catal* 2018; **8**: 2021–9.

15. Chen L, Guo Z and Wei XG *et al*. Molecular catalysis of the electrochemical and photochemical reduction of CO_2 with earth-abundant metal complexes. Selective production of CO vs HCOOH by switching of the metal center. *J Am Chem Soc* 2015; **137**: 10918–21.

16. Azcarate I, Costentin C and Robert M *et al*. Through-space charge interaction substituent effects in molecular catalysis leading to the design of the most efficient catalyst of CO_2-to-CO electrochemical conversion. *J Am Chem Soc* 2016; **138**: 16639–44.

17. Sheng H and Frei H. Direct observation by rapid-scan FT-IR spectroscopy of two-electron-reduced intermediate of tetraaza catalyst $[Co(II)N_4H(MeCN)]^{2+}$ converting CO_2 to CO. *J Am Chem Soc* 2016; **138**: 9959–67.

18. Nakajima T, Tamaki Y and Ueno K *et al*. Photocatalytic reduction of low concentration of CO_2. *J Am Chem Soc* 2016; **138**: 13818–21.

19. Windle CD, George MW and Perutz RN *et al*. Comparison of rhenium–porphyrin dyads for CO_2 photoreduction: photocatalytic studies and charge separation dynamics studied by time-resolved IR spectroscopy. *Chem Sci* 2015; **6**: 6847–64.

20. Tamaki Y, Koike K and Morimoto T *et al*. Red-light-driven photocatalytic reduction of CO_2 using Os(II)–Re(I) supramolecular complexes. *Inorg Chem* 2013; **52**: 11902–9.

21. Cheung PL, Kapper SC and Zeng T *et al*. Improving photocatalysis for the reduction of CO_2 through non-covalent supramolecular assembly. *J Am Chem Soc* 2019; **141**: 14961–5.

22. Windle CD and Perutz RN. Advances in molecular photocatalytic and electrocatalytic CO_2 reduction. *Coord Chem Rev* 2012; **256**: 2562–70.

23. Luo YH, Dong LZ and Liu J *et al*. From molecular metal complex to metal-organic framework: the CO_2 reduction photocatalysts with clear and tunable structure. *Coord Chem Rev* 2019; **390**: 86–126.

24. Yamazaki Y, Takeda H and Ishitani O. Photocatalytic reduction of CO_2 using metal complexes. *J Photochem Photobiol C* 2015; **25**: 106–37.

25. Takeda H, Ohashi K and Sekine A *et al*. Photocatalytic CO_2 reduction using Cu(I) photosensitizers with a Fe(II) catalyst. *J Am Chem Soc* 2016; **138**: 4354–7.

26. Rao H, Schmidt LC and Bonin J *et al*. Visible-light-driven methane formation from CO_2 with a molecular iron catalyst. *Nature* 2017; **548**: 74–7.

27. Thoi VS, Kornienko N and Margarit CG *et al*. Visible-light photoredox catalysis: selective reduction of carbon dioxide to carbon monoxide by a nickel n-heterocyclic carbene–isoquinoline complex. *J Am Chem Soc* 2013; **135**: 14413–24.

28. Shirley H, Su X and Sanjanwala H *et al*. Durable solar-powered systems with Ni-catalysts for conversion of CO_2 or CO to CH_4. *J Am Chem Soc* 2019; **141**: 6617–22.

29. Bonin J, Robert M and Routier M. Selective and efficient photocatalytic CO_2 reduction to CO using visible light and an iron-based homogeneous catalyst. *J Am Chem Soc* 2014; **136**: 16768–71.

30. Liu M, Mu YF and Yao S *et al*. Photosensitizing single-site metal—organic framework enabling visible-light-driven CO_2 reduction for syngas production. *Appl Catal B* 2019; **245**: 496–501.

31. Guo Z, Cheng S and Cometto C *et al*. Highly efficient and selective photocatalytic CO_2 reduction by iron and cobalt quaterpyridine complexes. *J Am Chem Soc* 2016; **138**: 9413–6.

32. Zhang HX, Hong QL and Li J *et al*. Isolated square-planar copper center in boron imidazolate nanocages for photocatalytic reduction of CO_2 to CO. *Angew Chem Int Ed* 2019; **58**: 11752–6.

33. Niu K, Xu Y and Wang H *et al*. A spongy nickel-organic CO_2 reduction photocatalyst for nearly 100% selective CO production. *Sci Adv* 2017; **3**: e1700921.

34. Hong D, Tsukakoshi Y and Kotani H *et al*. Visible-light-driven photocatalytic CO_2 reduction by a Ni(II) complex bearing a bioinspired tetradentate ligand for selective CO production. *J Am Chem Soc* 2017; **139**: 6538–41.

35. Ouyang T, Huang HH and Wang JW *et al*. A dinuclear cobalt cryptate as a homogeneous photocatalyst for highly selective and efficient visible-light driven CO_2 reduction to CO in CH_3CN/H_2O solution. *Angew Chem Int Ed* 2017; **56**: 738–43.

36. Ouyang T, Wang HJ and Huang HH *et al*. Dinuclear metal synergistic catalysis boosts photochemical CO_2-to-CO conversion. *Angew Chem Int Ed* 2018; **57**: 16480–5.

37. Boston DJ, Xu C and Armstrong DW *et al*. Photochemical reduction of carbon dioxide to methanol and formate in a homogeneous system with pyridinium catalysts. *J Am Chem Soc* 2013; **135**: 16252–5.

38. Zhao J, Wu W and Sun J *et al*. Triplet photosensitizers: from molecular design to applications. *Chem Soc Rev* 2013; **42**: 5323–51.

39. Zhao J, Ji S and Wu W *et al*. Transition metal complexes with strong absorption of visible light and long-lived triplet excited states: from molecular design to applications. *RSC Adv* 2012; **2**: 1712–28.

40. Harriman A, Hissler M and Khatyr A *et al*. A Ru(II) tris(2,2'-bipyridine) derivative possessing a triplet lifetime of 42 μs. *Chem Commun* 1999; 735–6.

41. Ji S, Wu W and Wu W *et al*. Ruthenium(II) polyimine complexes with a long-lived ^{3}IL excited state or a ^{3}MLCT/^{3}IL equilibrium: efficient triplet sensitizers for low-power upconversion. *Angew Chem Int Ed* 2011; **50**: 1626–9.

42. Tyson DS, Henbest KB and Bialecki J *et al*. Excited state processes in ruthenium(II)/pyrenyl complexes displaying extended lifetimes. *J Phys Chem A* 2001; **105**: 8154–61.

43. Guo S, Chen KK and Dong R *et al*. Robust and long-lived excited state Ru(II) polyimine photosensitizers boost hydrogen production. *ACS Catal* 2018; **8**: 8659–70.

44. Tsuji Y, Yamamoto K and Yamauchi K *et al*. Near-infrared light-driven hydrogen evolution from water using a polypyridyl triruthenium photosensitizer. *Angew Chem Int Ed* 2018; **57**: 208–12.

45. Wang P, Guo S and Wang HJ *et al.* A broadband and strong visible-light-absorbing photosensitizer boosts hydrogen evolution. *Nat Commun* 2019; **10**: 3155.

46. Ji S, Wu W and Wu W *et al.* Tuning the luminescence lifetimes of ruthenium(II) polypyridine complexes and its application in luminescent oxygen sensing. *J Mater Chem* 2010; **20**: 1953.

47. Zhang N, Chen KK and Guo S *et al.* Sensitizing Ru(II) polyimine redox center with strong light-harvesting coumarin antennas to mimic energy flow of biological model for efficient hydrogen evolution. *Appl Catal B* 2019; **253**: 105–10.

48. Lu Y, Wang J and McGoldrick N *et al.* Iridium(III) complexes bearing pyrene-functionalized 1,10-phenanthroline ligands as highly efficient sensitizers for triplet-triplet annihilation upconversion. *Angew Chem Int Ed* 2016; **55**: 14688–92.

49. Guo S, Wu W and Guo H *et al.* Room-temperature long-lived triplet excited states of naphthalenediimides and their applications as organic triplet photosensitizers for photooxidation and triplet-triplet annihilation upconversions. *J Org Chem* 2012; **77**: 3933–43.

50. Guo H, Muro-Small ML and Ji S *et al.* Naphthalimide phosphorescence finally exposed in a platinum(II) diimine complex. *Inorg Chem* 2010; **49**: 6802–4.

51. Indelli MT, Ghirotti M and Prodi A *et al.* Solvent switching of intramolecular energy transfer in bichromophoric systems: photophysics of (2,2′-bipyridine) tetracyanoruthenate(II) / pyrenyl complexes. *Inorg Chem* 2003; **42**: 5489–97.